Energy Storage Materials 78 (2025) 104250

Contents lists available at ScienceDirect

Energy Storage Materials

journal homepage: www.elsevier.com/locate/ensm

In-situ polymerization formed self-healing quasi-solid electrolyte for high-loading lithium batteries☆

Honghao Liu[a], Songteng Luo[a], Yuzi Yang[a], Xianming Zhao[a], Gaoxu Huang[a], Xiaopan Jin[a], Tianyu Zhong[a], Mengjia Guan[a,*], Jichang Liu[b,*], Yongsheng Li[a,b,**]

[a] Lab of Low-Dimensional Materials Chemistry, Key Laboratory for Ultrafine Materials of Ministry of Education, Frontier Science Center of the Materials Biology and Dynamic Chemistry, Shanghai Engineering Research Center of Hierarchical Nanomaterials, School of Materials Science and Engineering, East China University of Science and Technology, Shanghai 200237, China

[b] School of Chemistry and Chemical Engineering, State Key laboratory Incubation Base for Green Processing of Chemical Engineering, Shihezi University, Shihezi, 832003, China

ARTICLE INFO

Keywords:
Self-healing
Quasi-solid electrolyte
In-situ polymerization
High-loading electrodes
Lithium battery

ABSTRACT

High-energy-density lithium batteries face critical challenges including mechanical damage and poor electrode/electrolyte contact, which leads to discontinuous interfacial charge transfer and high interfacial resistance. To address these issues, a novel self-healing quasi-solid electrolyte (SHQSE) was synthesized through in-situ polymerization. The design employs hydroxyethyl acrylate as a molecular bridge to combine acrylates and polyurethanes with disulfide and complementary hydrogen bonds. These multiple dynamic bonds enable rapid Li^+ transport (7.2×10^{-4} S cm^{-1}) and enhanced self-healing capability. Furthermore, the excellent solid electrolyte/electrode interfacial contact is achieved during cycling through in-situ polymerization, and interfacial defects caused by polymer chain exchange and reorganization are effectively repaired. Consequently, capacity retention of 62.6 % in high-loading (>10 mg cm^{-2}) $LiFePO_4$ cells and 75.5 % in $LiNi_{0.8}Mn_{0.1}Co_{0.1}O_2$ cells after 500 cycles were obtained. Additionally, the self-healing polymer (SHP) functions as ion conductive agent, and continuous Li^+ transport paths formed within silicon carbon (Si/C) electrodes enable electrode integrity, achieving 74.5 % capacity retention over 200 cycles at 0.33 C. Moreover, the 2 Ah NCM811|Si/C@SHP soft pack battery with SHQSE exhibits an ultra-long cycle life and safety. This innovatively in-situ formed SHQSE offers an effective way for the development of high-performance solid-state batteries.

1. Introduction

The rapid development of electric vehicles and energy storage markets has created an urgent demand for efficient and safe lithium batteries. However, traditional lithium batteries face challenges such as low energy density and potential hazards, including leakage, volatility, and flammability. Therefore, the development of solid electrolytes with higher energy density, enhanced safety, and longer cycle life has become highly desirable for next-generation energy storage devices [1–4]. Solid electrolytes with high mechanical strength are believed to be the ultimate remedy to address safety issues. The formation of a solid-solid interface between inorganic solid electrolytes and electrodes typically induces two critical failure mechanisms: discontinuities in Li^+ transport and Li dendrite propagation. These coupled phenomena ultimately degrade battery cycle life through interfacial instability [5–8]. In contrast, solid polymer electrolytes (SPEs) offer advantages such as flexibility and good contact/adhesion with the electrodes. This improved interfacial contact enhances performance by ensuring continuous Li^+ transport and mitigating issues related to mechanical stress and deformation. However, batteries are subject to repeated deformation or even fracture due to external forces during practical applications [9,10]. During the cycling of lithium batteries, the volume

☆ Communication.

* Corresponding authors.

** Corresponding author at: Lab of Low-Dimensional Materials Chemistry, Key Laboratory for Ultrafine Materials of Ministry of Education, Frontier Science Center of the Materials Biology and Dynamic Chemistry, Shanghai Engineering Research Center of Hierarchical Nanomaterials, School of Materials Science and Engineering, East China University of Science and Technology, Shanghai 200237, China.

E-mail addresses: guanmj@ecust.edu.cn (M. Guan), liujc@ecust.edu.cn (J. Liu), ysli@ecust.edu.cn (Y. Li).

https://doi.org/10.1016/j.ensm.2025.104250
Received 16 December 2024; Received in revised form 24 March 2025; Accepted 8 April 2025
Available online 15 April 2025
2405-8297/© 2025 Elsevier B.V. All rights are reserved, including those for text and data mining, AI training, and similar technologies.

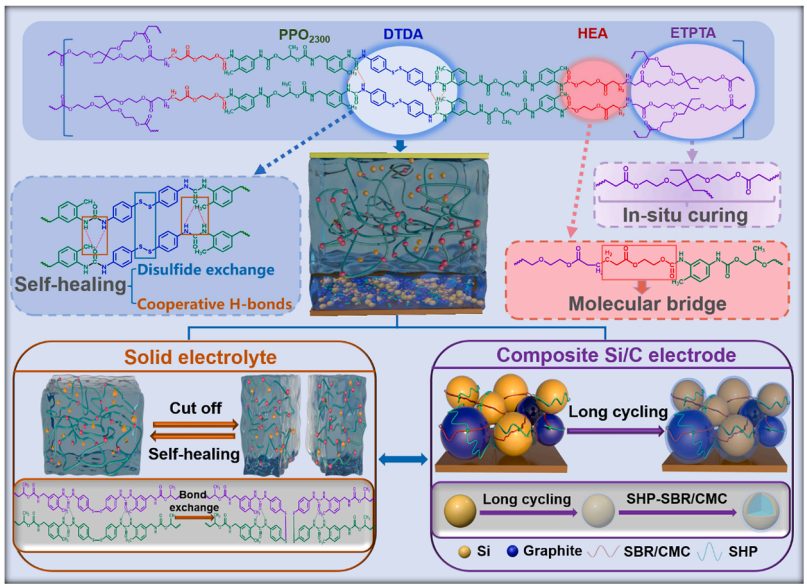

Fig. 1. Schematic representation of the SHP polymerization process, schematic structure of dynamic covalent disulfide and hydrogen bonds and the mechanism for the action of Si/C composite electrode.

expansion of electrode materials disrupts Li^+ transport, leading to a sudden decrease in battery capacity and premature battery failure [11,12].

Recent advances in solid-state battery research have highlighted the critical need to understand and mitigate interfacial instabilities between electrolytes and electrodes. Multiple degradation mechanisms, including chemical, electrochemical, and mechanical processes, manifest at polymer electrolyte/electrode interfaces, impacting both the electrolyte and electrode phases [13,14]. Various experimental strategies have been reported to enhance solid interfacial compatibility and mitigate the volume expansion of electrode materials for the development of solid-state lithium batteries. Recently, dynamic covalent bonds with self-healing functions and supramolecular interactions have been introduced into SPEs to improve their mechanical stability and flexibility [15,16]. Self-healing polymers possess intrinsic recovery properties at the molecular level through physical and chemical methods. Common self-healing mechanisms in solid electrolytes include hydrogen bonds [17,18], disulfide bonds [19,20], imine bonds [21,22], and transesterification [23,24]. Self-healing polymer electrolytes have demonstrated to significantly improve the cycling stability and safety of lithium batteries. Pu et al. [21] synthesized homogeneous and highly crosslinked gel electrolytes (PEGDA-UPy) with autonomous, fast self-healing, and a promising PF_5^- scavenging role. Similarly, Xie et al. [25] developed a crosslinked network (PDDP) that combines hydrogen and dynamic disulfide bonds. This network can achieve spontaneous repair of mechanical damage or microcracks formed during the assembly or cycling of lithium batteries. Thus, it can suppress electrode volume expansion and significantly enhance the cycling performance and safety of batteries. In recent years, research has predominantly focused on functional aspects of electrolytes, such as self-healing and flame retardancy. However, significant challenges remain at the interface between solid polymer electrolytes and porous electrodes, resulting in unstable interfacial ion transport and degraded electrochemical performance [26–28]. Therefore, enhancing the compatibility of the polymer solid electrolyte/electrode interface is crucial for improving the cycle life of lithium batteries.

In-situ polymerization strategies can effectively solve the interface problems of SPEs [7,29–31]. Ion transport at the electrode/electrolyte interface can be significantly enhanced by the in-situ formation of the dense and closely connected solid electrolyte layer [32–35]. For instance, Mai et al. [36] developed a topological polymer-based interface layer to regulate the high modulus and low interfacial activation energy of the Li metal solid electrolyte interface (SEI). To improve the Li^+ conductivity, Xue et al. [37] employed a one-step synthesis method to fabricate a block copolymer electrolyte (BCPE). This approach balanced Li^+ coordination properties and enabled rapid Li^+ transfer at the polymer electrolyte interface. Chen et al. [38] proposed a chemical/electrochemical reaction strategy leveraging the synergistic interaction between 1,4,7,10,13,16-hexaoxacyclooctadecane (18C6) and $LiNO_3$ for simultaneous in-situ construction of a stabilized cathode-anode interface. The unique $[18C6Li]^+NO_3^-$ cluster modifies the electric double-layer structure through specific adsorption on the electrode surface, effectively regulating interfacial layer composition. However, most of the solid electrolyte layers formed through in-situ curing strategies are inherently brittle and lack elasticity [39–42]. Following high-current cycling, the in-situ polymerized electrolyte tends to crack and without self-repair capability, causing safety issues such as short circuits, as it fails to withstand the stresses and strains of higher intensity [43,44]. Therefore, it is a key research focus for the construction of polymer electrolytes with fast Li^+ transport at the interface and the ability to inhibit electrode volume changes.

Herein, a self-healing polymer (SHP) with multiple dynamic bonds was developed through in-situ polymerization. The hydroxyethyl acrylate (HEA) works as the molecular bridge, and ethoxylated trimethylolpropane triacrylate (ETPTA) with crosslinking points improves the self-healing ability and mechanical strength of the electrolyte. Furthermore, the dithiodianiline (DTDA) provides dynamic covalent bonds, while poly(propylene glycol) (PPO_{2300}) extends chain segments and introduces complementary hydrogen bonds. Based on the excellent mechanical and self-healing properties of SHP, the self-healing quasi-solid electrolyte (SHQSE) was constructed by introducing liquid electrolytes (LE) into the SHP network through in-situ curing. The dynamic disulfide and complementary hydrogen bonds in the polymer chains were combined through in-situ polymerization. PPO_{2300} chain segments promote rapid Li^+ transport (7.2×10^{-4} S cm^{-1}), while alternating soft and hard segments from PPO_{2300} enhance the mechanical flexibility of the polymers. The in-situ polymerization strategy significantly enhances interfacial compatibility before cycling. During operation, the exchange and reorganization of SHQSE polymer chains effectively repair interfacial defects, ensuring sustained contact between the QSE and electrode while promoting uniform Li^+ deposition. SHP also acts as the ion conductive agent with its crosslinked network structure forming the

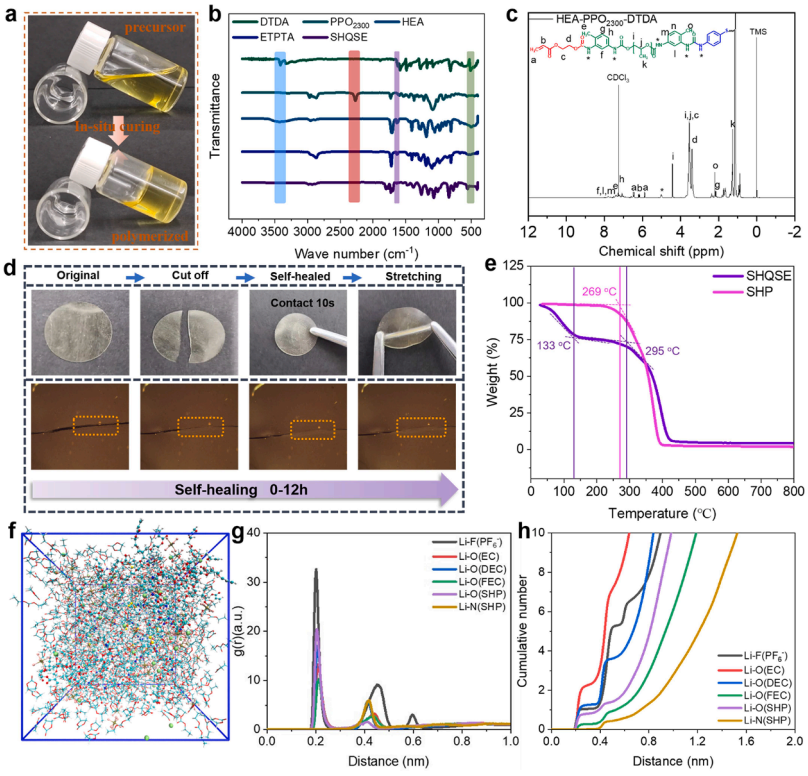

Fig. 2. (a) Physicochemical properties of the in-situ fabricated SHQSE. (b) FTIR spectra of the DTDA, PPO_{2300}, HEA, ETPTA and SHQSE. (c) ^{1}H NMR spectrum of the synthesized HEA-PPO_{2300}-DTDA in $CDCl_3$. (d) Photographs of the healing process of SHP at room temperature and the healing process under optical microscope. (e) Thermogravimetric analysis curves of SHQSE and SHP. (f) Snapshots of SHP molecular dynamics simulations in liquid electrolytes. (g) Radial distribution function of SHP and (h) coordination number.

continuous Li^{+} transport paths on silicon/carbon (Si/C) electrodes. Furthermore, the multiple dynamic bonds and crosslinked structures in the polymer chains reduce the stresses and strains caused by the silicon particles expansion, inhibiting the volume expansion of the electrode during cycling (Fig. 1 and Fig. S1). As a result, SHQSE demonstrates excellent electrochemical stability with Li metal and Si/C electrodes during long-term cycling. Additionally, composite Si/C electrodes and SHQSE are integrated together to prepare a 2 Ah soft pack battery that exhibit 87 % capacity retention after 400 cycles and demonstrate high tolerance to abusive conditions. This approach provides a novel perspective for improving the performance of lithium batteries using QSEs.

2. Results and discussion

2.1. In-situ synthesis of SHQSE and MD simulations

SHQSE was synthesized by the polymerization of monomers containing abundant polar functional groups with high affinity for Li^{+}. As shown in Fig. 2a, there is no significant change in color before and after polymerization; the solution remains yellow and transparent in both states, indicating that the secondary thermal polymerization process had no effect on the system. The chemical composition of SHQSE and raw materials was analyzed by Fourier transform infrared spectroscopy (FTIR) (Fig. 2b). PPO_{2300} exhibits a distinct -NCO characteristic peak at 2277 cm^{-1}, while DTDA shows an N—H stretching peak at 3326 cm^{-1}. Characteristic peaks of HEA and ETPTA appears at 3409 cm^{-1} (-OH) and 1635 cm^{-1} (C=C), respectively. After polymerization, these peaks largely disappeared in SHQSE, though weak C=C peaks persist, suggesting residual unreacted ETPTA monomers. This may result from a polymerization inhibitor in ETPTA slowing the reaction rate, leading to oligomer formation. The disulfide bond is confirmed by a new peak at 560 cm^{-1}. The peak of the C=O group (1727 cm^{-1}) (Fig. S2) is split into two peaks, with one shifting to around 1695 cm^{-1}, attributed to hydrogen bonding between NH—COO, indicating the presence of intermolecular hydrogen bonds in the system, which further enhance the self-healing capability. The ^{1}H NMR and ^{12}C NMR spectra recorded with $CDCl_3$ as solvent elucidated the structural compositions of PPO_{2300}-DTDA and PPO_{2300}-DTDA-HEA (Fig. 2c and Fig. S3, 4). In ^{12}C NMR, peaks at 127.7 ppm (-NCO) and 139.3 ppm (-NH—C(pH)-) confirm residual -NCO and urea group formation in PPO_{2300}-DTDA. For HEA-PPO2300-DTDA, ^{1}H NMR peaks at 5.83, 6.41 and 6.12 ppm correspond to -CH=CH_2 groups, while the absence of a peak at 3.86 ppm verifies successful HEA incorporation. Conversion rates were calculated via ^{1}H NMR (Fig. S5): 81 % of ETPTA and HEA-PPO_{2300}-DTDA reacted, leaving 19 % unreacted monomers or oligomers, confirming successful crosslinking. An optimal crosslinking degree enhances mechanical strength and ion mobility.

The self-healing ability of SHP was assessed by inflicting physical injury using a hobby knife (Fig. 2d). When the cut surfaces were recontacted, SHP withstood 10-second external stimuli at room temperature without rupture. Optical microscope images show that the fractured surfaces healed after 12 h at room temperature. This indicates that SHP has strong self-healing ability due to the combination of dynamic disulfide bonds and complementary hydrogen bonds. Due to the in-situ curing process, SHQSE's self-healing could not be directly observed. Therefore, a non-in-situ method was used: SHP was immersed in liquid electrolyte (LE) to form SHP-LE (Fig. S6). The experimental results show that the self-healing time of SHP-LE is longer compared to SHP, indicating that the electrolyte (LE) weakens the self-healing ability. To further demonstrate the stable operation of SHQSE at high temperatures, self-healing experiments were performed at 60 °C (Fig. S7). The self-healing performance exhibits a significant temperature dependence: at 60 °C, SHP achieves complete crack closure within 6 h (compared to 12 h at 25 °C). Tensile tests (Fig. S8) revealed the mechanical hierarchy:

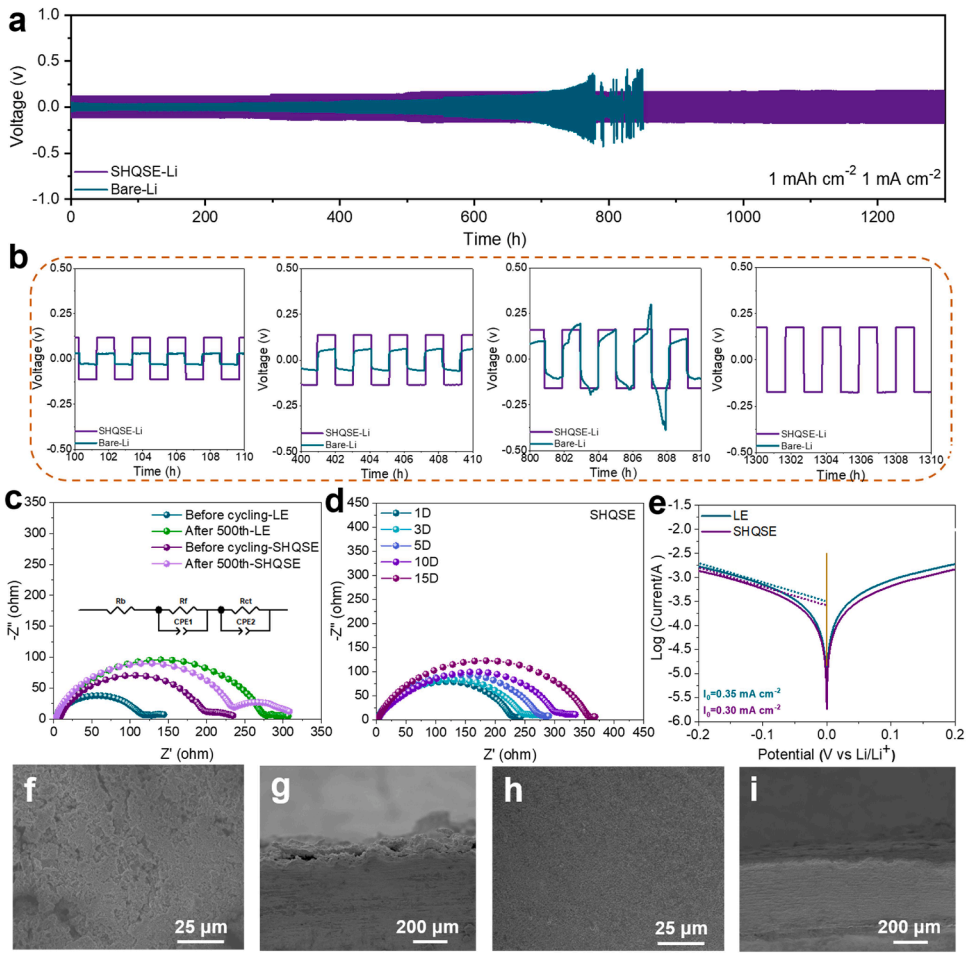

Fig. 3. Electrochemical properties of ultrathin SHQSE and LE in symmetric Li|Li cells at 25 °C. (a) Long-term cycling performance of Li|Li symmetric cells in SHQSE and LE at 1 mA cm^{-2} and 1 mAh cm^{-2} and magnification over different time periods (b). (c) EIS plots of Li|Li symmetric cells before and after 500 cycles in SHQSE and LE. (d) EIS plot of Li|Li symmetric cells impedance with the variation of time (1–15 days) for SHQSE. (e) Tafel curves of Li|Li symmetric cells with SHQSE and LE. SEM images of the Li metal anodes after 500 cycles in (f-g) LE and (h-i) SHQSE.

SHP > SHP-LE, with reduced strength and strain due to LE-induced disruption of crystalline domains and weakened interchain interactions [45]. Despite this, SHQSE retains sufficient self-healing ability for electrochemical stability applications.

The DSC results of SHQSE and SHP show that the glass transition temperature (Tg) of SHQSE was −54.4 °C (Fig. S9) with a crystalline melting temperature (Tm) of 119.5 °C. The Tg and Tm of SHP were −35.8 and 96.3 °C, respectively. These results indicate that the incorporation of LE in SHQSE lowers its Tg [46]. The low Tg disordered crosslink network structure enhances segment mobility in SHQSE, which is beneficial for Li^+ transport and ionic conductivity [47]. As shown in Fig. 2e, SHP demonstrates remarkable thermal stability with an initial decomposition onset temperature of 269 °C. In contrast, SHQSE displays a distinct two-stage degradation pattern: (1) Due to the high volatility of LE, SHQSE exhibits an obvious weight loss from room temperature to 133 °C [48]; (2) The subsequent decomposition of the polymer matrix begins at 295 °C, which indicates that SHQSE possesses higher thermal stability than LE [49].

To further investigate the solvation structure of the electrolytes, NMR tests were conducted on SHQSE and LE. The NMR was used to examine the local environments of Li^+ and F^- in $LiPF_6$. As shown in Fig. S10, the SHQSE exhibits a downshift from −0.75 ppm to −0.59 ppm compared to LE, indicating that the weaker electronegative environment around Li^+ promotes Li^+ migration [11]. The ^{19}F NMR shows that the peak of SHQSE gradually shifts to the lower field, indicating that the crosslinked network restricts PF_6^--polymer interactions, thereby weakening the electron shielding around F atoms. SHQSE contains an amount of LE, while the solid electrolyte was cured inside the battery by in-situ polymerization. Therefore, LE was always present throughout the system, and molecular dynamics simulations were quite challenging due to the large molecular weight of SHQSE. Traditional molecular dynamics (MD) simulations were conducted to analyze the interactions between Li^+ and the components of the electrolyte system. These simulations aimed to further investigate the coordination environment of Li^+ in both SHP and LE. Fig. 2f displays a simulated snapshot of SHP in LE, illustrating the uniform distribution of ions and solvent molecules throughout the simulation framework. The radial distribution functions (RDF) and coordination numbers (CN) reveal Li^+ solvation shell composition. As shown in Fig. 2 g, h, there are five Li^+ coordination pairs at approximately 0.2 nm, corresponding to Li-O (EC), Li-O (SHP), Li-O (DEC), Li-F (PF_6^-), and Li-O (FEC), indicating the involvement of SHP in the solvation shell of Li^+. The average CN values are 2.25 (EC), 1.26 (DEC), 1.06 (PF_6^-), 0.82 (O-SHP), 0.45 (N-SHP), and 0.27 (FEC), demonstrating that SHP reduces PF_6^- coordination in LE. In the local structure (Fig. S11), Li^+ migrates within SHP accompanied by solvent molecules, indicating that Li^+ preferentially coordinates with SHP's O atoms to form additional transport channels. Hydrogen bond analysis (Fig. S12, Table S1) shows that 15 SHP molecules form 8.3 intra-SHP hydrogen bonds on average, consistent with the C=O blue shift in FTIR. Due to the presence of C=O or O in EC, FEC, and DEC, all of these molecules can form hydrogen bonds with LE to varying degrees, thereby encapsulating the LE.

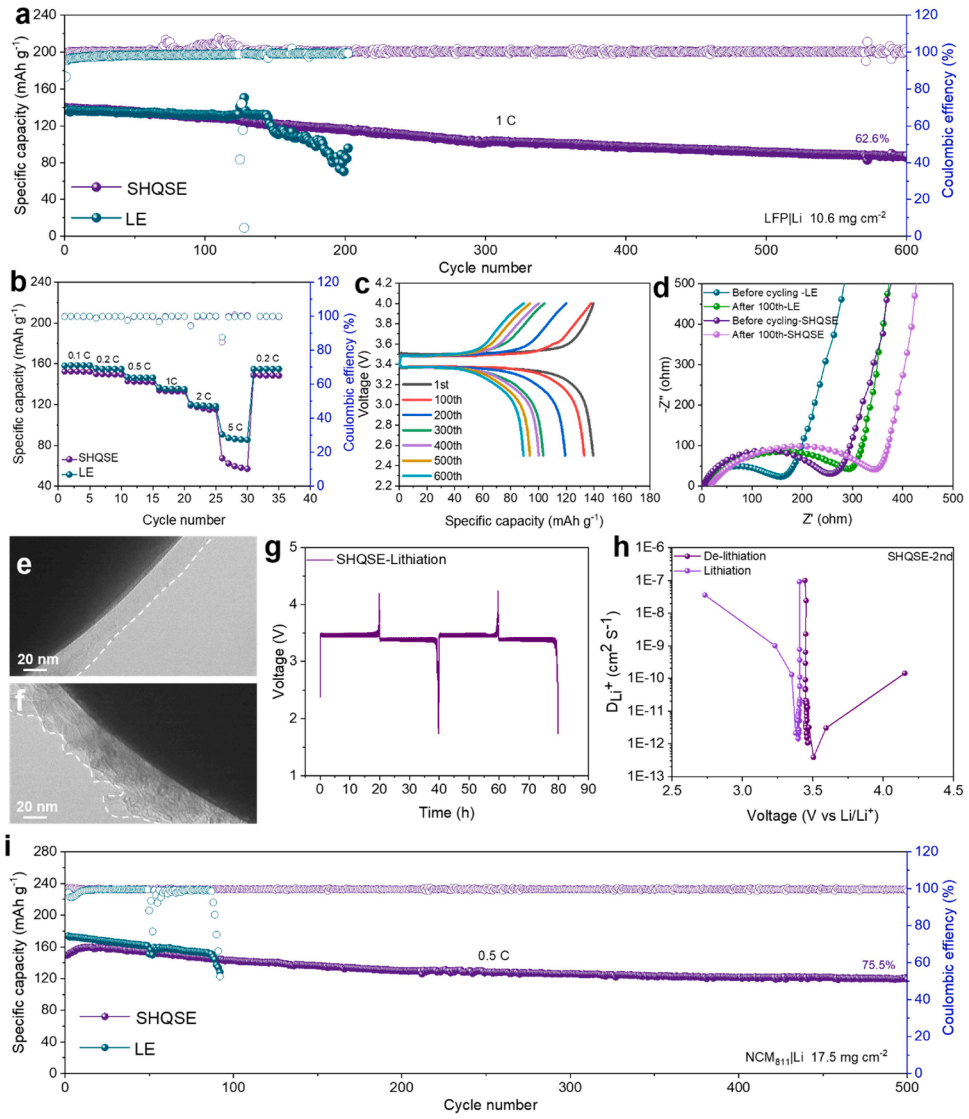

Fig. 4. Electrochemical performance of full cells with high loading using SHQSE and LE. (a) Cycling performance of Li|LFP full cells in SHQSE and LE at 1 C. (b) Rate capacities of Li|LFP full cells. (c) The corresponding capacity curves in SHQSE for different number of cycles of charging/discharging. (d) EIS plots of SHQSE and LE for LFP full cells before and after the 100th cycle. (e) High-resolution TEM images of LFP particles after 100 cycles of SHQSE and (f) LE. (g) GITT profiles at the discharge/charge process (SHQSE), diffusion coefficients calculated from GITT profiles (h). (i) Cycling performance of Li|NCM811 full cells in SHQSE and LE at 0.5 C.

The linear sweep voltammetry (LSV) tests were conducted to investigate the oxidative stability of the materials and assess their feasibility for high-voltage cathodes. Using LE as the reference, the electrochemical characterization revealed that the oxidation current rises sharply at ~4.5 V (SHQSE) and ~4.4 V (LE), indicating irreversible electrolyte decomposition at these potentials (Fig. S13). The stability of LE is primarily attributed to the relatively stable molecular structure of FEC. In contrast, the crosslinked network structure (urethane groups) of SHP effectively stabilizes polymer chain segments against oxidative decomposition. The strong electrostatic interactions and hydrogen bonding of LE with the SHP network enhance structural stability and retard the decomposition of $LiPF_6$, thereby conferring excellent electrochemical stability to SHQSE [50]. As shown in Fig. S14, SHQSE exhibits a non-corrosive effect on Li metal in comparison with LE, indicating that the overall polymer structure provides excellent Li stability without significant side reaction. Comparing to LE (36.63°) (Fig. S15), the contact angle of SHQSE is 41.54° and the complex structure of the system increases the viscosity, resulting in slightly lower wettability than that of LE. Nevertheless, the contact angle of SHQSE is still better than that of other polymeric solid electrolytes and does not affect the wettability of the diaphragm and electrodes [51]. The Li^+ conductivity properties of SHQSE and LE from 30 to 80 °C are presented in Fig. S16. The Li^+ conductivity of LE is slightly higher than that of SHQSE (30 °C, 0.95 > 0.72 mS cm^{-1}). This indicates that the viscosity of the system increases before crosslinking, and the enhanced crosslinked structure, further reduces Li^+ conductivity. With the increase in temperature (70–80 °C), the Li^+ conductivity of SHQSE becomes greater than that of LE. This phenomenon arises because the crystalline region of SHQSE decreases at high temperatures, while enhanced polymer activity further contributes to the significant improvement in Li^+ conductivity. SHQSE exhibits a higher Li^+ migration number ($t_{Li}^+ = 0.56$), which is attributed to the reduced interaction of Li^+ with the solvent, leading to more free migration of Li^+. The abundant hydrogen bonds and crosslinking network hinder anion migration to some extent, inhibiting the formation of space charge near the Li anode and further reducing the dendrite formation under high current density (Fig. S17). Comparative Li|SS cell tests (Fig. S18) demonstrate that SHQSE achieves comparable current peaks and charge transfer characteristics to LE during Li stripping/-plating. These results confirm that SHQSE maintains excellent electrochemical kinetics while improving cycling stability.

2.2. Li stripping/plating reversibility and stability

The compatibility between SHQSE and Li anode plays a critical role in determining the performance of high-energy-density Li metal batteries. The surface of the Li electrode was protected by an in-situ formed self-healing layer. The self-healing capabilities of SHQSE were further investigated by testing Li|Li symmetric cells. For comparison, the cell with LE was also tested under the conditions of 1 mA cm^{-2} and 1 mAh cm^{-2}. As shown in Fig. 3a-b, the symmetric cell with SHQSE exhibits excellent interfacial compatibility and electrochemical stability, achieving a cycling life of 1300 h and a stable overpotential of 120 mV. This performance is significantly better than that of the LE-based symmetric cell and surpasses many reported solid electrolytes (Table S2). The polarization tests (Fig. S19) conducted at different current densities (3 mA cm^{-2} and 5 mA cm^{-2}) show stable cycling of 3500 h and 650 h with consistent overpotential, indicating that the electrolyte can be used under high-current conditions in batteries. In addition, the interfacial impedance of the Li|Li symmetric cell with SHQSE increases by 38 Ω after 500 cycles, while that of LE increases by 118 Ω at 1 mA cm^{-2} (Fig. 3c). The impedance variation over time shows that the interfacial impedance of SHQSE increased from 225 Ω on the first day to 356 Ω on the 15th day, while that of LE increased from 311 Ω to 476 Ω (Fig. 3d and Fig. S20). Furthermore, the rapid Li^+ transfer kinetics at the Li electrode/electrolyte interface were demonstrated by Tafel plots of Li|Li symmetric cells. As shown in Fig. 3e, the exchange current density for SHQSE (0.3 mA cm^{-2}) is slightly lower than that for LE (0.35 mA cm^{-2}), suggesting that high compatibility between the in-situ form SHQSE and the Li anode may facilitate rapid Li^+ transfer.

SEM was employed to observe the Li deposition morphologies using different electrolytes. The Li|Li symmetric cell was disassembled after 500 cycles at current densities of 1 mA cm^{-2} and 1 mAh cm^{-2}. For LE (Fig. 3f, g and Fig. S21a, b), Li deposition is uneven and accompanied by severe corrosion. The Li metal surface exhibits an irregular dendritic structure, indicating significant voltage hysteresis and instability, and poor cycling performance. In contrast, the Li surface in SHQSE exhibits a smooth and dense depositional morphology without visible cracks. (Fig. 3h, i and Fig. S21c, d). The self-healing interface helps maintain the integrity of the SEI and reduce interfacial side reactions. This uniform and dense Li deposition behavior in SHQSE ensures more stable Li stripping/plating reversibility and further improves the electrochemical performance of practical Li metal batteries.

X-ray photoelectron spectroscopy (XPS) characterization was performed on cycled Li metal from Li|Li symmetric cells after 50 cycles to determine the SEI composition. As shown in Fig. S22, the surfaces of LE and SHQSE are dominated by C—C/C—H, C—O/C=O, and C-F species in the C 1 s and O 1 s spectra, which are characteristic of organic species compounds primarily derived from solvent decomposition (EC, DEC, and FEC). The decrease in contents etching depth indicates that the SEI outer layer is rich in organic components, while the inner layer is dominated by inorganic components. This structure improves ionic conductivity and mechanical stability, thereby inhibiting lithium dendrite generation [52]. In the F 1 s spectra, the SEI of SHQSE shows higher LiF contents in both the inner and outer layers compared to LE. The C-F content in the inner layer of SHQSE SEI is slightly increased, which benefits for enhancing SEI conductivity. Notably, $LiPF_6$ and FEC generate C-F and LiF, but $LiPF_6$ produces more side reactions and forms a loose SEI layer, while FEC directly forms a dense LiF-rich SEI [53]. Meanwhile, the content of LixPOyFz derived from $LiPF_6$ is lower in SHQSE's SEI than in LE, confirming that LiF originates from FEC decomposition. The crosslinked network structure of SHQSE hinders the movement of PF_6^-, reduces direct contact with Li metal, and inhibits $LiPF_6$ decomposition [54]. Remarkably, the Li_2O content on the surface of SHQSE is higher than that of LE. This is attributed to the unsaturated double bonds in the residual monomers (such as ETPTA), which are prone to be reduced because of their low LUMO (Fig. 5b). Consequently, this reduction process leads to forming more Li_2O on the surface [55]. This inorganic-rich SEI isolates Li from electrolyte corrosion, improving reversibility and stability. The S 2p spectra reveal S-S bonds in the SEI, enriching its composition and enhancing anode stability.

2.3. Practical applications in LFP and NCM811 cells

To demonstrate the capability of SHQSE in practical applications, Li metal full cells were assembled with high-loading cathodes: $LiFePO_4$ (LFP, areal loading: 10.6 mg cm^{-2}) and $LiNi_{0.8}Co_{0.1}Mn_{0.1}O_2$ (NCM811, areal loading: 17.5 mg cm^{-2}). As shown in Fig. 4a, the Li|LE|LFP cell delivers an initial discharge capacity of 137 mAh g^{-1} at 1 C. After 147 cycles, the specific capacity begins abrupt decay, reaching 70 mAh g^{-1} by the 200th cycle. In contrast, the Li|SHQSE|LFP cell maintains a reversible discharge capacity of 87 mAh g^{-1}, with over 99 % coulombic efficiency and 62.6 % capacity retention after 600 cycles, outperforming most reported solid-state batteries (Table S2). The rate performance of the integrated Li|LFP cell was evaluated at different current densities ranging from 0.1 to 5 to 0.2 C (Fig. 4b). The specific capacities of SHQSE and LE are comparable from 0.1 to 2 C, and they even exhibit similar specific capacities at 1 C and 2 C. When the current density returns to 0.2 C, the capacity returns to its initial level. The dynamic disulfide bonds and the numerous complementary hydrogen bonds in SHQSE are proven to be highly reversible and the in-situ curing enhances the contact between SHQSE and the LFP electrode/electrolyte interface. Additionally, the charge/discharge curves of the full cell using SHQSE at 1 C for different cycles show excellent cycling performance, without significant increase in overpotential observed over 600 cycles (Fig. 4c).

The electrochemical impedance spectra (EIS) of both cells before and after cycling are shown in Fig. 4d After 100 cycles, the impedance of the LFP with LE increases by 138 Ω, while the interfacial impedance of SHQSE increases by 87 Ω. This increase is mainly attributed to the formation of stable self-healing interfaces between SHQSE and the electrodes after cycling. The cathode electrolyte interface (CEI) is an important component affecting the cathode/electrolyte interface, and the formation process of CEI can be understood by high-resolution transmission electron microscopy. As shown in Fig. 4e, the Li|SHQSE|LFP cell forms a uniform amorphous layer (CEI) on the surface of LFP material particles after 100 cycles. In contrast, the LFP material particles with LE form the thicker and inhomogeneous CEI layer, resulting in the higher interfacial resistance at the cathode/solid electrolyte interface (Fig. 4f). The Li^+ diffusion coefficient (D_{Li}^+) was further calculated using the galvanostatic intermittent titration technique (GITT). As shown in Fig. 4 g, h and Fig. S23, the Li^+ diffusion coefficients of Li|SHQSE|LFP in the lithiation and delithiation states are approximately the same as those of Li|LE|LFP (Fig. S24). These results are consistent with the Tafel analysis. The excellent diffusion kinetics and cyclic reversibility are further demonstrated [56]. Finally, the high-voltage cycling stability performance was evaluated using a high-loading NCM811 cathode. As shown in Fig. 4i and Fig. S25, the capacity of the Li|LE|NCM811 cell continues to drop at 0.5 C and suddenly failed at the 87th cycle due to uneven Li deposition and rapid growth of Li dendrites. In contrast, Li|SHQSE|NCM811 cell maintains a stable capacity of 120.9 mAh g^{-1} capacity and 75.5 % capacity retention after 500 cycles. The results demonstrate excellent cycling performance compared to other works listed in Table S2. The high reversibility of SHQSE at different rates from 0.1 to 5 to 0.2 C further verifies its self-healing and high-voltage resistance properties (Fig. S26). As shown in the C 1 s spectra of Fig. S27, both LE and SHQSE systems exhibit organic species including C—C/C—H, C—O, O—C=O, and C-F components, which originate from electrolyte decomposition. Notably, the content of these organic components decreases progressively with increasing etching depth. This trend indicates that the CEI structure resembles the conventional SEI architecture, featuring an organic-rich outer layer and an inorganic-dominated inner layer. The F 1 s spectra further reveal that the SHQSE system contains a higher LiF content compared to the LE system, along with C-F and LixPOyFz species in both cases. These species

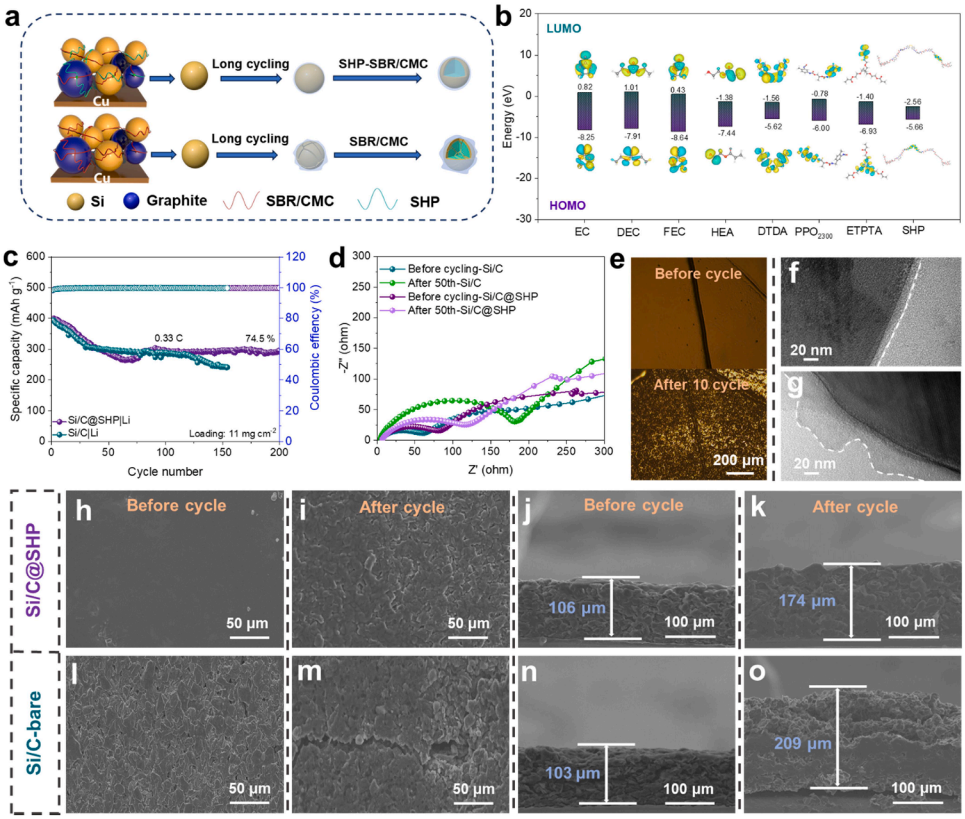

Fig. 5. (a) Schematic representation of particle changes after long cycling in Si/C and Si/C@SHP. (b) HOMO and LUMO energy levels of different molecular and SHP. (c) Cycling performance of different Li|Si/C cells at 0.33 C. (d) EIS plots of Si/C@SHP and Si/C for Li|Si/C cells before and after 50 cycles. (e) Scratched composite Si/C@SHP electrode and optical microscope image after ten cycles. (f) Si/C@SHP and (g) Si/C high-resolution TEM images of Si/C anode particles after 50 cycles. Top-view SEM images of Si/C@SHP (h) and (l) Si/C electrodes before cycling. Top-view SEM images of Si/C@SHP (i) and Si/C (m) electrodes after 50 cycles. Cross-sectional SEM images of Si/C@SHP (j) and Si/C (n) electrodes before cycling. Cross-sectional SEM images of Si/C@SHP (k) and Si/C (o) electrodes after 50 cycles.

are likely derived from the decomposition of $LiPF_6$ because of the lower HOMO energy level of FEC and the resistance to decomposition. With increasing etching depth, LixPOyFz still exists in the LE system, providing additional evidence that the LiF possibly originates from $LiPF_6$ decomposition. In addition, the LiF in both the outer and inner layers of the CEI in the SHQSE system is lower than that in the LE system, suggesting that SHQSE inhibits $LiPF_6$ decomposition [54]. The O 1 s spectra show that the SHQSE system has higher lattice oxygen content and a lower surface oxygen content with increasing etching depth compared to LE. This finding indicates that SHQSE generates a thinner CEI, which is consistent with the conclusions drawn from TEM observations and long-term cycling experiments. Moreover, the S 2p spectra reveal the presence of S-S in both the inner and outer layers at 163.6 eV, suggesting that SHQSE participates in CEI layer formation. Thus, SHQSE enhances the compatibility between the electrode and electrolyte, suppresses further decomposition, and enables fast and uniform Li^+ transport in the cell.

2.4. Practical applications in Si/C cells

The functionality and availability of SHP were further verified with schematic diagrams showing the post-cycling state of silicon particles in Si/C electrode materials (Fig. 5a). SHP was introduced into the electrode material as the ionic conductive agent. The crosslinked network formed efficient Li^+ transport channels through in-situ polymerization. Simultaneously, polymer chains adhered to the surface of the anode material particles, optimizing the Li^+ transport path between them. The complex soft and hard chain segments combined with dynamic self-healing covalent bonds synergistically constructed a polymer network to withstand high stresses and form elastic protective layers. The oxidation stability of the solid electrolyte is a significant indicator in practical applications. Fig. 5b presents the HOMO and lowest unoccupied molecular orbital (LUMO) energy levels of different molecules obtained from density functional theory (DFT) calculations. FEC has lower LUMO and HOMO compared to other solvent molecules (EC, DEC), indicating its preferential decomposition of FEC at the anode and enhanced oxidative stability. The solid electrolyte monomer contains unstable groups (e.g. C=C). Upon in-situ polymerization, SHP forms a crosslinked network structure that enables more uniform dispersion of the negative electron region, which interacts with the LE to enhance oxidative stability. This finding is consistent with the results of LSV [57]. In the SHQSE system, more Li^+ clusters are generated due to the increased LE encapsulation around the solid electrolyte, inducing additional LiF formation, as confirmed by XPS [50]. The Li^+ conductive network dissociates Li salts and induces the formation of stable SEI, which inhibits side reactions at the electrode/solid electrolyte interface and provides excellent interfacial stability. The elemental mapping images (Fig. S28) show that the Si/C electrode contains C and Si elements, with uniformly distributed S elements at low concentrations on the surface and within the electrode. The Li|Si/C@SHP cell exhibits 74.5 % capacity retention after 200 cycles at 0.33 C (Fig. 5c). Owing to SHP's self-healing properties and fast Li^+ transport channels, the capacity recovers after 70 cycles. This unique advantage is attributed to the adaptive and self-healing capability of the composite anode, where SHP builds robust networks on the surface of the particles. The alternating soft and hard segments of the polymer can tolerate volume changes in silicon to maintain mechanical and electrochemical integrity. The EIS curves (Fig. 5d) show that the interfacial impedance of the Si/C@SHP cell increases by only 39 Ω after 50 cycles at 0.33 C, whereas that of the Li|Si/C cell rises sharply by 184 Ω. Fig. 5e shows the self-healing of Li|

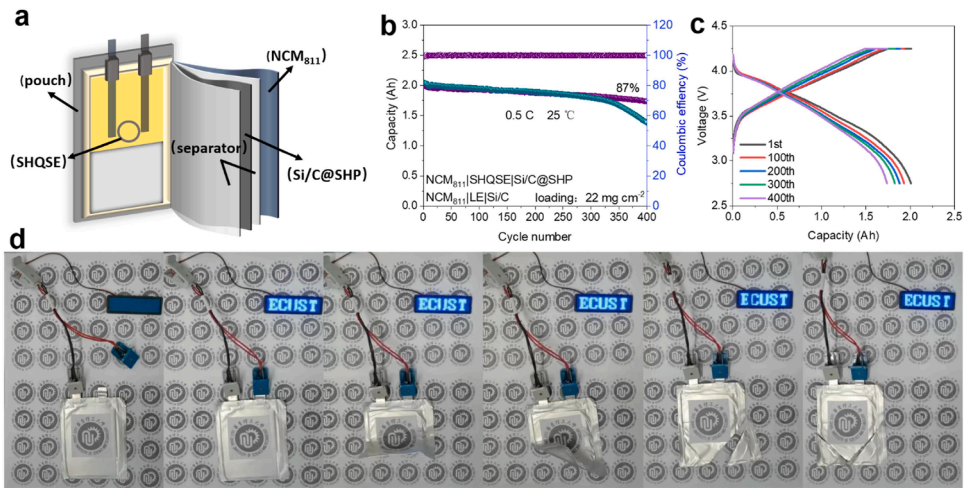

Fig. 6. Construction, flexibility and safety demonstration of the NCM811|SHQSE|Si/C@SHP soft pack batteries. (a) Schematic of the NCM811|SHQSE|Si/C@SHP soft pack battery structure. (b) Cycling performance of 2 Ah NCM811|SHQSE|Si/C@SHP and NCM811|LE|Si/C soft pack batteries at 0.5 C and 25 °C. (c) Voltage-Capacity Curves of NCM811|SHQSE|Si/C@SHP soft pack batteries with different number of turns. (d) Optical photographs of NCM811|SHQSE|Si/C@SHP soft pack battery lighting up a light sign at 25 °C under different states and destructive conditions.

Si/C@SHP electrodes before and after cycling. The apparent healing of the scratches can be attributed to self-healing mechanisms of SHP during the cycling process. As shown in Fig. 5h-k, the Si/C@SHP electrode remains smooth and dense with minimal cracking and thickness increase after cycling, confirming SHP's ability to suppress volume expansion. In contrast, the Si/C electrode with the styrene butadiene rubber/-carboxymethyl cellulose sodium (SBR/CMC) (Fig. 5l-o) shows severe surface cracks, particle fragmentation, and doubled electrode thickness due to inadequate stress tolerance. These results indicate that SHP significantly improves the overall performance of Si/C electrodes through structural and interfacial stabilization, making it possible to apply polymer electrolyte as the ionic conductive agent.

2.5. Practical applications of soft pack batteries

The practicality of highly-load positive and negative materials in SHQSE was successfully verified. This was achieved through an in-situ SHQSE polymerization strategy, which enabled the assembly of a 2 Ah NCM811|SHQSE|Si/C@SHP soft pack battery. The structure and detailed design diagram of the NCM811|SHQSE|Si/C@SHP soft pack battery are schematically presented in Fig. 6a and Fig. S29. The cycle stability of the soft pack battery was tested at 25 °C (Fig. 6b). The NCM811|SHQSE|Si/C@SHP soft pack battery initially delivers a capacity of 2 Ah at 0.5 C and maintains 87 % capacity after 400 cycles. In comparison, the LE-based soft pack battery retains 69 % capacity under identical cycling conditions. The capacity-voltage curves show that SHQSE maintains high capacity performance even after long cycling, with negligible changes (Fig. 6c). The LE-based battery exhibits significant polarization voltage fluctuations in the later stages of cycling, leading to rapid capacity decay (Fig. S30). The SHQSE integrated soft pack battery achieves enhanced cycle stability through interfacial self-healing and adaptive volume expansion. The light board continues to function without burning or smoking despite multiple 90° folds and destructive experiments (e.g., cutting the package), demonstrating exceptional safety and flexibility. These results confirm that SHQSE-based solid-state batteries possess excellent practical safety value.

3. Conclusion

In summary, we developed a self-healing quasi-solid electrolyte with multiple dynamic bonds formed through in-situ polymerization, which significantly improved self-healing efficiency and mechanical strength. The SHQSE, synthesized via in-situ thermal polymerization of ETPTA, HEA, DTDA and PPO_{2300}, not only repairs interfacial defects but also improves the solid electrolyte/electrode interfacial contact to ensure uniform Li^+ deposition. The formation of dynamic disulfide bonds and complementary hydrogen bonds in the polymer chain through in-situ polymerization endows SHQSE with high stretchability and Li^+ conductivity. Additionally, SHP serves as an ionic conductive agent for Si/C electrodes. Its complex crosslinked network enables SHP to create continuous Li^+ transport paths on Si/C electrodes, thereby alleviating the stresses caused by the expansion of silicon particles. Benefiting from these advantages, the in-situ polymerized SHQSE cells exhibit smaller voltage polarization and impedance, more uniform and flat electrode interfaces, and excellent cycling performance compared to LE. The NCM811|SHQSE|Si/C@SHP soft pack battery demonstrates stable cycling (87 % capacity retention after 400 cycles), robust flexibility without electrochemical degradation under folding, and excellent safety under abuse conditions with no short-circuiting or combustion. These results highlight its great potential for practical applications. This in-situ strategy combined with self-healing capabilities highlights the potential of SHQSE to advance safe and high-performance lithium batteries.

CRediT authorship contribution statement

Honghao Liu: Writing – original draft, Visualization, Methodology, Investigation. **Songteng Luo:** Visualization. **Yuzi Yang:** Methodology, Investigation. **Xianming Zhao:** Formal analysis. **Gaoxu Huang:** Methodology, Formal analysis. **Xiaopan Jin:** Data curation. **Tianyu Zhong:** Data curation. **Mengjia Guan:** Writing – review & editing. **Jichang Liu:** Supervision. **Yongsheng Li:** Writing – review & editing, Supervision, Funding acquisition, Conceptualization.

Declaration of competing interest

The authors declare that they have no known competing financial interests or personal relationships that could have appeared to influence the work reported in this paper.

Acknowledgements

The authors acknowledge the financial supports from Shanghai Pilot Program for Basic Research (22TQ1400100-13), the Leading Talents in Shanghai in 2018 and the 111 project (B14018).

Supplementary materials

Supplementary material associated with this article can be found, in the online version, at doi:10.1016/j.ensm.2025.104250.

References

[1] Q. Lv, C. Li, Y. Liu, Y. Jing, J. Sun, H. Wang, L. Wang, H. Ren, B. Cheng, T. Wu, D. Wang, In-situ polymerized high-voltage solid-state lithium metal batteries with dual-reinforced stable interfaces, ACS Nano 18 (2024) 23253–23264.

[2] H. Li, D. Wu, J. Wu, L.Y. Dong, Y.J. Zhu, X. Hu, Flexible, high-wettability and fire-resistant separators based on hydroxyapatite nanowires for advanced lithium-ion batteries, Adv. Mater. 44 (2017) 1703548.

[3] K. Pan, L. Zhang, W. Qian, X. Wu, K. Dong, H. Zhang, S. Zhang, A flexible ceramic/polymer hybrid solid electrolyte for solid-state lithium metal batteries, Adv. Mater. 17 (2020) 2000399.

[4] J. Wang, K. Wang, Y. Xu, Emerging two-dimensional covalent and coordination polymers for stable lithium metal batteries: from liquid to solid, ACS Nano 12 (2021) 19026–19053.

[5] Z. Li, L. Wang, M. Yu, Y. Liu, B. Liu, Z. Sun, W. Hu, Lithium-rich porous aromatic framework doped quasi-solid polymer electrolyte for lithium battery with high cycling stability, ACS Appl. Mater. Interfaces 48 (2022) 53798–53807.

[6] K. Fu, Y. Gong, G.T. Hitz, D.W. McOwen, Y. Li, S. Xu, Y. Wen, L. Zhang, C. Wang, G. Pastel, J. Dai, B. Liu, H. Xie, Y. Yao, E.D. Wachsman, L. Hu, Three-dimensional bilayer garnet solid electrolyte based high energy density lithium metal-sulfur batteries, Energy Environ. Sci. 7 (2017) 1568–1575.

[7] Q. Zhao, X. Liu, S. Stalin, K. Khan, L.A. Archer, Solid-state polymer electrolytes with in-built fast interfacial transport for secondary lithium batteries, Nat. Energy 4 (2019) 365–373.

[8] J. Wan, J. Xie, D.G. Mackanic, W. Burke, Z. Bao, Y. Cui, Status, promises, and challenges of nanocomposite solid-state electrolytes for safe and high-performance lithium batteries, Mater. Today Nano 4 (2018) 1–16.

[9] W. Tang, S. Tang, C. Zhang, Q. Ma, Q. Yang, Y.W. Yang, J. Luo, Simultaneously enhancing the thermal stability, mechanical modulus, and electrochemical performance of solid polymer electrolytes by incorporating 2D sheets, Adv. Energy Mater. 24 (2018) 1800866.

[10] Q. Han, S. Wang, L. Wang, W. Ren, F. Zhang, J. Lu, H. Wang, Exploiting iodine redox chemistry for achieving high-capacity and durable PEO-Based all-solid-state $LiFePO_4$/Li batteries, Adv. Energy Mater. 13 (2023) 2301462.

[11] Y. Jiang, Y. Song, X. Chen, H. Wang, L. Deng, G. Yang, In situ formed self-healable quasi-solid hybrid electrolyte network coupled with eutectic mixture towards ultra-long cycle life lithium metal batteries, Energy Storage Mater. 52 (2022) 514–523.

[12] Y. Huang, Z. Shi, H. Wang, J. Wang, Z. Xue, Shape-memory and self-healing polyurethane-based solid polymer electrolytes constructed from polycaprolactone segment and disulfide metathesis, Energy Storage Mater. 51 (2022) 1–10.

[13] Z. Li, H. Zhang, X. Sun, Y. Yang, Mitigating interfacial instability in polymer electrolyte-based solid-state lithium metal batteries with 4 V cathodes, ACS Energy Lett. 5 (2020) 3244–3253.

[14] K. Yang, J. Ma, Y. Li, J. Jiao, S. Jiao, X. An, G. Zhong, L. Chen, Y. Jiang, Y. Liu, D. Zhang, Weak-interaction environment in a composite electrolyte enabling ultralong-cycling high-voltage solid-state lithium batteries, J. Am. Chem. Soc. 16 (2024) 11371–11381.

[15] Z. Li, J. Fu, S. Zheng, D. Li, X. Guo, Self-healing polymer electrolyte for dendrite-free li metal batteries with ultra-high-voltage ni-rich layered cathodes, Small 17 (2022) 2200891.

[16] D.G. Mackanic, X. Yan, Q. Zhang, N. Matsuhisa, Z. Yu, Y. Jiang, T. Manika, J. Lopez, H. Yan, K. Liu, X. Chen, Y. Cui, Z. Bao, Decoupling of mechanical properties and ionic conductivity in supramolecular lithium-ion conductors, Nat. Commun. 1 (2019) 5384.

[17] B. Li, F. Wang, F. Hu, T. Ding, P. Huang, X. Xu, J. Liang, C. Li, Q. Zhou, M. Lu, L. Deng, L. Guo, W. Cui, Injectable "Nano-micron" combined gene-hydrogel microspheres for local treatment of osteoarthritis, NPG Asia Mater. 1 (2022) 14.

[18] R. Tamate, Y. Peng, Y. Kamiyama, K. Nishikawa, Extremely Tough, Stretchable gel electrolytes with strong interpolymer hydrogen bonding prepared using concentrated electrolytes to stabilize lithium-metal anodes, Adv. Mater. 22 (2023) 2211679.

[19] D.D. Zhang, Y.B. Ruan, B.Q. Zhang, X. Qiao, G. Deng, Y. Chen, C.Y. Liu, A self-healing PDMS elastomer based on acylhydrazone groups and the role of hydrogen bonds, Polymer (Guildf) 120 (2017) 189–196.

[20] P. Wang, L. Yang, B. Dai, Z. Yang, S. Guo, G. Gao, L. Xu, M. Sun, K. Yao, J. Zhu, A self-healing transparent polydimethylsiloxane elastomer based on imine bonds, Eur. Polym. J. 123 (2020) 109382.

[21] L. Zhang, P. Zhang, C. Chang, W. Guo, Z.H. Guo, X. Pu, Self-healing solid polymer electrolyte for room-temperature solid-state lithium metal batteries, ACS Appl. Mater. Interfaces 13 (2021) 46794.

[22] K. Deng, S. Zhou, Z. Xu, M. Xiao, A high ion-conducting, self-healing and nonflammable polymer electrolyte with dynamic imine bonds for dendrite-free lithium metal batteries, Chem. Eng. J. 428 (2022) 131224.

[23] R.H. Grubbs, Olefin metathesis tetrahedron, 60(2004), 7117.

[24] B. Zhou, T. Deng, C. Yang, M. Wang, H. Yan, Z. Yang, Z. Wang, Z. Xue, Self-healing and recyclable polymer electrolyte enabled with boronic ester transesterification for stabilizing ion deposition, Adv. Funct. Mater. 13 (2023) 2212005.

[25] K. Chen, Y. Sun, X. Zhang, J. Liu, H. Xie, A self-healing and nonflammable cross-linked network polymer electrolyte with the combination of hydrogen bonds and dynamic disulfide bonds for lithium metal batteries, Energy Environ. Sci. 4 (2023) e12568.

[26] W.P. Wang, J. Zhang, J. Chou, Y.X. Yin, Y. You, S. Xin, Y.G. Guo, Solidifying cathode-electrolyte interface for lithium-sulfur batteries, Adv. Energy Mater. 2 (2021) 2000791.

[27] F. Pei, L. Wu, Y. Zhang, Y. Liao, Q. Kang, Y. Han, H. Zhang, Y. Shen, H. Xu, Z. Li, Y. Huang, Interfacial self-healing polymer electrolytes for long-cycle solid-state lithium-sulfur batteries, Nat. Commun. 1 (2024) 351.

[28] D. Dong, B. Zhou, Y. Sun, H. Zhang, G. Zhong, Q. Dong, F. Fu, H. Qian, Z. Lin, D. Lu, Y. Shen, J. Wu, L. Chen, H. Chen, Polymer electrolyte glue: a universal interfacial modification strategy for all-solid-state li batteries, Nano Lett. 4 (2019) 2343–2349.

[29] Y.G. Cho, C. Hwang, D.S. Cheong, Y.S. Kim, H.K. Song, Gel/solid polymer electrolytes characterized by in situ gelation or polymerization for electrochemical energy systems, Adv. Mater. 20 (2019) 1804909.

[30] J. Chai, Z. Liu, J. Ma, J. Wang, X. Liu, H. Liu, J. Zhang, G. Cui, L. Chen, In situ generation of poly (vinylene carbonate) based solid electrolyte with interfacial stability for $LiCoO_2$ lithium batteries, Adv. Sci 2 (2017) 1600377.

[31] K. Mu, D. Wang, W. Dong, Q. Liu, Z. Song, W. Xu, P. Yao, Y.A. Chen, B. Yang, C. Li, L. Tian, C. Zhu, J. Xu, Hybrid crosslinked solid polymer electrolyte via in-situ solidification enables high-performance solid-state lithium metal batteries, Adv. Mater. 47 (2023) 2304686.

[32] F.Q. Liu, W.P. Wang, Y.X. Yin, S.F. Zhang, J.L. Shi, L. Wang, X.D. Zhang, Y. Zheng, J.J. Zhou, L. Li, Y.G. Guo, Upgrading traditional liquid electrolyte via in situ gelation for future lithium metal batteries, Sci. Adv. 4 (2018) eaat5383.

[33] Q. Lu, C. Wang, D. Bao, H. Duan, F. Zhao, K. Doyle-Davis, Q. Zhang, R. Wang, S. Zhao, J. Wang, H. Huang, X. Sun, High-performance quasi-solid-state pouch cells enabled by in situ solidification of a novel polymer electrolyte, Energy Environ. Mater. 4 (2023) e12447.

[34] J. Xiang, Y. Zhang, B. Zhang, L. Yuan, X. Liu, Z. Cheng, Y. Yang, X. Zhang, Z. Li, Y. Shen, J. Jiang, Y. Huang, A flame-retardant polymer electrolyte for high performance lithium metal batteries with expanded operation temperature, Energy Environ. Sci. 14 (2021) 3510–3521.

[35] Y. Wang, S. Chen, Z. Li, C. Peng, Y. Li, W. Feng, In-situ generation of fluorinated polycarbonate copolymer solid electrolytes for high-voltage li-metal batteries, Energy Storage Mater. 45 (2022) 474–483.

[36] H. Xu, J. Zhang, H. Zhang, J. Long, L. Xu, L. Mai, Situ topological interphases boosting stable solid-state lithium metal batteries, Adv. Energy Mater. 21 (2023) 2204411.

[37] K. Guo, J. Wang, Z. Shi, Y. Wang, X. Xie, Z. Xue, One-step in situ polymerization: a facile design strategy for block copolymer electrolytes, Angew. Chem. Int. Ed 9 (2023) e202213606.

[38] C. Zhao, Y. Lu, K. Yan, Y. Guan, S. Jiang, J. Wang, S. Guo, Tailoring the chemical/electrochemical response in a quasi-solid polymer electrolyte enables the simultaneous in situ construction of superior cathodic and anodic interfaces, Adv. Energy Mater. 22 (2024) 2304532.

[39] S. Randau, D.A. Weber, O. Kotz, R. Koerver, P. Braun, A. Weber, E. Ivers-Tiffee, T. Adermann, J. Kulisch, W.G. Zeier, F.H. Richter, J. Janek, Benchmarking the Performance of all-solid-state lithium batteries, Nat. Energy 3 (2020) 259–270.

[40] D. Lei, K. Shi, H. Ye, Z. Wan, Y. Wang, L. Shen, B. Li, Q.H. Yang, F. Kang, Y.B. He, Progress and perspective of solid-state lithium-sulfur batteries, Adv. Funct.l Mater. 38 (2018) 1707570.

[41] H. Xu, H. Zhang, J. Ma, G. Xu, T. Dong, J. Chen, G. Cui, Overcoming the challenges of 5 V spinel $LiNi_{0.5}Mn_{1.5}O_4$ cathodes with solid polymer electrolytes, ACS Energy Lett. 12 (2019) 2871–2886.

[42] H. Zhang, L. Huang, H. Xu, X. Zhang, Z. Chen, C. Gao, C. Lu, Z. Liu, M. Jiang, G. Cui, A polymer electrolyte with a thermally induced interfacial ion-blocking function enables safety-enhanced lithium metal batteries, Escience 2 (2022) 201–208.

[43] A. Sanchez-Sanchez, J.A. Pomposo, Single-chain polymer nanoparticles via non-covalent and dynamic covalent bonds, Part. Part. Syst. Char. 1 (2014) 11–23.

[44] J. Xu, J. Chen, Y. Zhang, T. Liu, J. Fu, A fast room-temperature self-healing glassy polyurethane, Angew. Chem. Int. Ed. 14 (2021) 7947–7955.

[45] X. Deng, J. Chen, X. Jia, X. Da, Y. Zhao, Y. Gao, X. Kong, S. Ding, G. Gao, Highly tough slide-crosslinked gel polymer electrolyte for stable lithium metal batteries, Angew. Chem. Int. Ed. 21 (2024) e202410818.

[46] G. Wang, X. Zhu, A. Rashid, Z. Hu, P. Sun, Q. Zhang, L. Zhang, Organic polymeric filler-amorphized poly(ethylene oxide) electrolyte enables all-solid-state lithium-metal batteries operating at 35 °C, J. Mater. Chem. A 26 (2020) 13351–13363.

[47] H. Wang, Q. Wang, X. Cao, Y. He, K. Wu, J. Yang, H. Zhou, W. Liu, X. Sun, Thiol-branched solid polymer electrolyte featuring high strength, toughness, and lithium ionic conductivity for lithium-metal batteries, Adv. Mater. 37 (2020) 2001259.

[48] X. Cheng, C. Lu, X. Gong, C. Li, J. Wang, J. Qu, Y. Zhang, T. Song, Y. Zhang, H. Jiang, C. Wang, Quasi-solid fiber-shaped lithium-ion batteries with fire resistance, Angew. Chem. Int. Ed. (2025) e202423419.

[49] L. Xue, H. Pan, Y. Wang, Z. Wang, X. Wang, Q. Lin, K. Zhang, X. Bu, M. Bai, B. Hong, A flame-retardant and weakly solvated gel electrolyte for high-performance and high-safety Ah class sodium-ion batteries, Chem. Eng. J. 504 (2025) 158828.

[50] C. Guo, Y. Guo, S. Yao, R. Tao, X. Liu, J. Wang, H. Li, H. Li, C. Hong, J. Geng, X. G. Sun, Multifunctional nitrile additives for inducing pseudo-concentration gel-polymer electrolyte: enabling stable high-voltage lithium metal batteries, Energy Storage Mater 71 (2024) 103683.

[51] A. Wang, Y. Tu, S. Wang, H. Zhang, F. Yu, Y. Chen, D. Li, PEGylated chitosan as gel polymer electrolyte for lithium ion batteries, Polymers (Basel) 21 (2022) 4552.

[52] B. Jagger, M. Pasta, Solid electrolyte interphases in lithium metal batteries, Joule 7 (2023) 2228–2244.
[53] P. Bai, X. Ji, J. Zhang, W. Zhang, S. Hou, H. Su, M. Li, T. Deng, L. Cao, S. Liu, X. He, Formation of LiF-rich cathode-electrolyte interphase by electrolyte reduction, Angew. Chem. Int. Ed. (61) (2022) e202202731.
[54] F. Liu, J. Wang, W. Chen, M. Yuan, Q. Wang, R. Ke, G. Zhang, J. Chang, C. Wang, Y. Deng, J. Wang, Polymer-ion interaction prompted quasi-solid electrolyte for room-temperature high-performance lithium-ion batteries, Adv. Mater. 36 (2024) 2409838.
[55] C. Guo, K. Du, R. Tao, Y. Guo, S. Yao, J. Wang, D. Wang, J. Liang, S.Y. Lu, Inorganic filler enhanced formation of stable inorganic-rich solid electrolyte interphase for high performance lithium metal batteries, Adv. Funct. Mater. 33 (2023) 2301111.
[56] Y. Guo, X. Liao, P. Huang, P. Lou, Y. Su, X. Hong, Q. Han, R. Yu, Y.-C. Cao, S. Chen, High reversibility of layered oxide cathode enabled by direct Re-generation, Energy Storage Mater. 43 (2021) 348–357.
[57] M.Le Nguyen, V.C. Nguyen, Y.L. Lee, J.S. Jan, H. Teng, Synergistic combination of ether-linkage and polymer-in-salt for electrolytes with facile Li^+ conducting and high stability in solid-state lithium batteries, Energy Storage Mater. 65 (2024) 103178.